IOP Publishing New J. Phys. 26 (2024) 113017 https://doi.org/10.1088/1367-2630/ad8f5b

New Journal of Physics
The open access journal at the forefront of physics

Deutsche Physikalische Gesellschaft DPG
IOP Institute of Physics

Published in partnership with: Deutsche Physikalische Gesellschaft and the Institute of Physics

OPEN ACCESS

RECEIVED
20 September 2024

REVISED
29 October 2024

ACCEPTED FOR PUBLICATION
6 November 2024

PUBLISHED
22 November 2024

PAPER

Attosecond emission delay from atoms and molecules using multi-dimensional XUV interferometry

Adam S Wyatt[1], **David T Lloyd**[2], **Richard T Chapman**[1], **Christopher Thornton**[1], **Paulina Majchrzak**[1], **Alfred J H Jones**[1], **Emma Springate**[1] and **Kevin O'Keeffe**[3,*]

[1] Central Laser Facility, STFC Rutherford Appleton Laboratory, Harwell OX11 0QX, United Kingdom
[2] Clarendon Laboratory, Department of Physics, University of Oxford, Parks Road, Oxford OX1 3PU, United Kingdom
[3] Faculty of Science and Engineering, Department of Physics, Swansea University, Singleton Park, Swansea SA2 8PP, United Kingdom
[*] Author to whom any correspondence should be addressed.

E-mail: k.okeeffe@swansea.ac.uk

Keywords: attoscience, interferometry, high-harmonic generation

Supplementary material for this article is available online

Abstract

Multi-dimensional interferometry of high harmonic generation is demonstrated using an inline Gouy interferometer. The rich data sets acquired with this technique, coupled with its inherent stability, enable robust phase analysis to be performed, allowing the delay in harmonic emission from a range of atomic and molecular gases to be measured relative to harmonic emission from argon with single-digit attosecond precision. Delays of -78 ± 6 as, -25 ± 6 as, 30 ± 3 as and 60 ± 3 as relative to emission from argon were measured for Xe, Kr, CO_2 and N_2, respectively. The scheme can easily be incorporated in other high harmonic experiments, such as tomographic imaging of molecular orbitals, and provides an experimentally simple route towards probing ultrafast dynamics in molecular systems.

1. Introduction

High harmonic generation (HHG) is an established method for producing coherent, extreme ultraviolet (XUV) radiation with attosecond pulse durations [1] and provides unique opportunities for spectroscopy of molecular systems [2, 3]. The well-known three-step model can be used to describe the process which produces high order harmonics [4]. First, an intense laser field ionizes an atom. The liberated electron is then accelerated away from and then towards the parent ion by the same laser field. Finally, the electron may recombine with the ground state of the parent ion, resulting in the emission of a photon of energy $E_q = q\hbar\omega_0$, where q is an odd integer and ω_0 is the fundamental laser frequency.

The emitted XUV field can be defined as a sum over various laser-driven quantum trajectories, each depending on a phase factor due to propagation of the electron wavepacket in the continuum, as well as the dipole transition moments during ionization and recombination; consequently, the emitted field provides a snapshot of the orbital structure of the generating species on a sub-laser-cycle timescale (i.e. 10 s to 100 s of attoseconds). HHG-based spectroscopy has therefore emerged as a powerful tool for extracting structural and dynamical information from molecular systems that can complement existing spectroscopic techniques. For example, the chirp inherent in the electron wavepacket during propagation and recombination provides a map between harmonic order and recollision time, which has previously been exploited to probe the nuclear dynamics of molecular hydrogen and deuterium, as well as small organic molecules [5, 6]. Since the propagation of the electron wavepacket is governed by the driving laser field, a high degree of spatial selectivity is possible between the ionization and recombination states involved in HHG that has been previously been utilized to perform tomographic imaging of aligned molecules [7, 8]. More recently, HHG-based spectroscopy has allowed a host of ultrafast phenomena in molecules to be observed in realtime including charge migration and transfer [9], electron–hole dynamics after strong-field ionization [10], and electronic, vibrational and rotational dynamics [11]. However, in most HHG experiments, only the intensity

of the harmonic spectrum is recorded, with the loss of phase information severely limiting the ability to fully reconstruct the state of the system. Retrieving the phase of the harmonic emission, which is important for extracting structural and dynamical information from harmonic spectra [12], is therefore a crucial requirement towards realising the full potential of HHG-based spectrocopy.

Interferometry is a proven method for characterising both the spatial and temporal phase of HHG sources. In the spatial domain, techniques such as multi-slit interference [13, 14], lateral shearing interferometry [15], spatially-encoded interferometry [16] and mutual interferometric characterization [17] have been used to determined the spectrally-resolved spatial phase of HHG emission. Methods to access temporal phase information have incorporated the use of two transversely separated laser foci in the generation region [18, 19], harmonic generation using a single beam in a mixture of noble gases [20], symmetry breaking of the HHG process in multi-colour fields [21], interference of two-photon transitions [22], as well as transversely separated beams in gas mixtures [23]. Recently, interference between harmonics generated in two gas targets, each located at one of two longitudinally-separated foci produced by a piezo-controlled segmented mirror, was demonstrated [24]. Compared with other techniques, this approach has the significant advantage that the signal strength and species in each arm of the interferometer can be varied independently, providing direct insight into fundamental processes such as tunnel-ionization [25, 26], laser-Coulomb coupling [27] and circular dichroism [28].

The XUV interferometer demonstrated here also comprises two longitudinally-separated gas targets. However, harmonics from both targets are generated within a single focus [29–31]. In this arrangement, the phase of harmonics generated at both target positions is different due to the smooth variation of the laser intensity and Gouy phase through the focal region, resulting in interference between harmonics generated in each target. In this paper, we demonstrate that by extending the parameter space of such a Gouy-based HHG interferometer it is possible to perform multi-dimensional interferometry from which the harmonic phase can be extracted with sub-wavelength precision, allowing the direct measurement of HHG emission delays from a range of atomic and molecular gases relative to a reference gas. This approach is straightforward to implement in existing HHG beamlines, provides single-digit attosecond precision, and is naturally compatible with pump-probe and tomographic imaging schemes, therefore opening a new route towards ultrafast spectrosopy of complex molecular systems.

A schematic of the interferometer is illustrated in figure 1(a). A laser beam is apertured slightly prior to focusing using a mechanical iris. The phase of harmonics generated at each target is given approximately by [32, 33]

$$\phi_q(z,r) \approx q\phi_{\mathrm{G}}(z) - \alpha_q^j I(r,z) + \psi_q \tag{1}$$

where $\phi_{\mathrm{G}}(z) \approx -z/z_{\mathrm{R}}$ is the Gouy phase after irising the beam, z is the longitudinal position, z_{R} is the Rayleigh range of the driving beam, r is the transverse coordinate, $I(r,z)$ is the laser intensity, α_q^j is a parameter related to the propagation time of the electron wavepacket in the continuum, which differs for the long ($j=l$) and short ($j=s$) quantum trajectories, and ψ_q is the phase acquired during ionization and recombination. Since the on-axis intensity, $I(0,z)$, varies relatively slowly with z through the focal region, the phase difference between both sources in this region is dominated by $\phi_{\mathrm{G}}(z)$, corresponding to a position-dependent delay between harmonics generated at each source. For two HHG sources in the focal region, where one source is fixed in position and the second is separated longitudinally from the first by Δz, the Gouy phase results in a delay in harmonic emission between the sources given by $\Delta t \approx q\Delta z/\omega_0 z_{\mathrm{R}}$. The resulting interference between harmonics generated in each target manifests as strong modulations in the spectrally-resolved harmonic intensity as Δz is varied. In a typical HHG experiment, z_{R} is of the order of millimetres and target positions can reliably be moved with sub-millimetre precision, such that delay steps of a few attoseconds are readily achievable. Indeed, the inherent synchronization of this scheme has previously enabled the demonstration of harmonic interference with unprecedented zeptosecond (10^{-21} s) temporal stability [29], the measurement of the harmonic phase difference between isotopes of molecular hydrogen [30], as well as the observation of interference between the separate components of the harmonic emission corresponding to the long and short quantum trajectories [31].

Previous implementations of HHG-based Gouy interferometry have only accessed limited regions of the available parameter space: the $(\Delta z,\omega)$ domain [29, 30], and the $(\Delta z,\omega,R)$ domain [31], where R is the transverse coordinate at the detector plane. In this paper, an extension of the approach taken in [31] is demonstrated, whereby the expanded parameter space of the interferometer, corresponding to the (z_1,z_2,ω,R) domain, is accessed by recording the spatially-resolved harmonic spectrum as a function of both target positions, where z_1 and z_2 are the longitudinal positions of the first and second target positions, respectively. This approach yields a significantly richer data set that allows us to unambiguously distinguish phase contributions from the long and short trajectories independently that are not attributable to

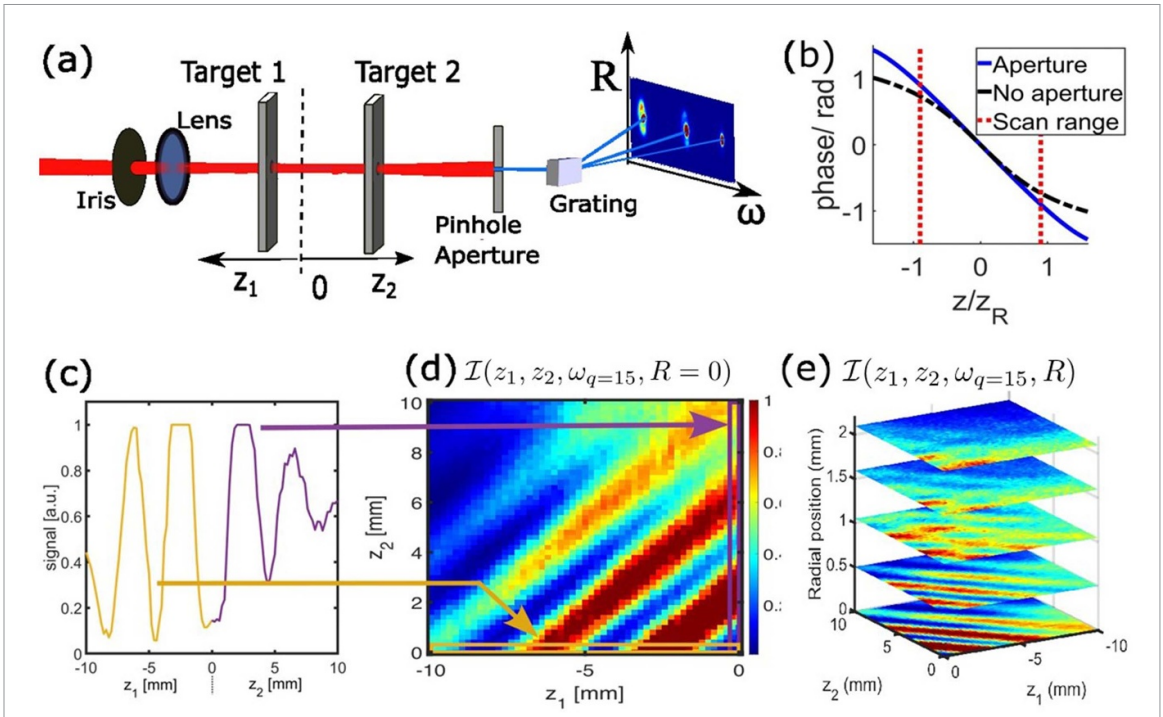

Figure 1. (a) Experimental setup. The spatio-spectrally resolved harmonic profiles are recorded for a range of target positions, z_1 and z_2. (b) Calculated on-axis phase variation of the driving laser through the focus with (blue line) and without (black dashed line) clipping from iris aperture. (c) Yellow (purple) line: Modulations in the on-axis ($R = 0$) harmonic intensity for $q = 15$ as the longitudinal separation between the first (second) target is varied while keeping the second (first) target fixed at position $z = 0$. (d) On-axis ($R = 0$) interferogram for $q = 15$ in the (z_1, z_2) domain. The yellow and purple boxes highlight the regions corresponding to the data shown in (c). (e) Evolution of the (z_1, z_2) interferograms for $q = 15$ for increasing values of R.

phase-matching or diffraction [34, 35]. Extending the concept to molecules could allow the contributions from different parent atoms to be isolated. The details of this will be left to a follow-on paper, and in this publication we concentrate on the on-axis ($R = 0$) component (dominated by a single trajectory) to demonstrate how the harmonic emission delay from a range of atomic and molecular gases relative to a target gas can be measured directly from the resulting interferograms.

2. Experimental setup

The output of a Ti:sapphire laser system (KMLabs Dragon) operating at 1 kHz and centre wavelength 780 nm was focused into a vacuum chamber using an achromatic lens with a focal length $f = 750$ mm. The pulse duration on target was approximately 40 fs and pulse energy was 310 μJ. The interferometer consisted of two gas targets placed in the focal region and along the propagation axis of the Ti:sapphire beam, as illustrated in figure 1(a). Both gas targets consisted of thin-walled nickel tubes, squeezed to a thickness of approximately 0.6 mm, and sealed at one end. The first (laser side) and second (spectrometer side) gas targets were each mounted to computer-controlled encoded translation stages, allowing the independent control of z_1 and z_2. Gas exit holes were drilled through both targets *in situ* by the laser beam, and at the beginning of the experiment each target was scanned about the focal region to open the exit holes and ensure that there was no clipping of the fundamental, or harmonic beams. The first and second gas targets were backed with argon to a pressure of 8 mbar and 4 mbar, respectively, such that the strength of harmonic emission from both targets was balanced. The small pressure difference between targets can be attributed to a slight difference in the thickness and size of the exit holes of each target, while the low pressures used ensured that phase-matching, ionization and absorption effects in both targets were minimized. The spatially-resolved harmonic spectrum was recorded using a custom-built spectrometer composed of an aberration-corrected concave grating (Hitachi: 001–0640) and microchannel plate (MCP) coupled to a phosphor screen, which was then imaged with a CCD camera. A 1 mm diameter aperture was placed between the target chamber and spectrometer to maintain the low pressure needed for operating the MCP, which was positioned approximately 0.7 m from the laser focus. With gas in both targets, strong modulations in the harmonic spectrum were observed as the longitudinal position of the gas targets was varied. In order to optimize the modulations, the laser beam was apertured slightly using a mechanical iris placed before the focusing lens, resulting in approximately 75% power transmission through the iris and a measured Rayleigh range of

approximately $z_R = 9$ mm. The effect of the iris can be seen in figure 1(b), which shows the calculated Gouy phase across the focus with (blue line) and without (black dashed line) aperturing the beam. The effect of the iris was calculated by propagating the apertured beam from the lens to the focal place via the Fresnel approximation and then propagating the beam about the focus using the angular spectrum method. The iris plays an important role in the interferometer as it results in a linear on-axis phase variation, as seen in figure 1(b), resulting in high-contrast interference fringes across the entire scan.

To record the intensity of the four-dimensional interferograms, $\mathcal{I}(z_1, z_2, \omega, R)$, both targets were placed near the focus of the laser beam. The longitudinal positions of both targets were then scanned over the ranges $z_1 = -10 - 0$ mm and $z_2 = 0 - 10$ mm. The position $z_1 = z_2 = 0$ mm corresponded to the case where both targets were adjacent to each other close to the focus of the laser and with a small displacement (≈ 1 mm) between the targets. The spatio-spectral HHG profile was recorded at each combination of target positions with a full scan consisting of 2601 (51×51) separate spectra, corresponding to a longitudinal resolution of 0.2 mm in both z_1 and z_2. The exposure times during each scan ranged from 100 ms to 300 ms depending on gas target. Concatenation of the recorded HHG profiles allows the $\mathcal{I}(z_1, z_2, \omega, R)$ interferograms to be constructed.

3. Results and discussion

Results from a scan with argon in both gas targets are shown in figures 1(c)–(e). In figure 1(c), two lineouts are shown, corresponding to the on-axis ($R = 0$) 1-D interference similar to data recorded in previous implementations of Gouy-based HHG interferometry [29–31] in which a single gas target is scanned longitudinally through the focus while the other is held fixed in position. Although strong on-axis modulations are observed, this approach accesses a significantly reduced portion of the available parameter space, limiting the information that can be extracted. By utilizing the full parameter space of the interferometer a much richer phase landscape is accessible, enabling more precise phase analysis of the measured interferograms to be performed. The full 4D interferograms also represent complex data sets which can be used as a rigorous test of theoretical models.

Figure 1(c) shows the on-axis ($R = 0$) component of $\mathcal{I}(z_1, z_2, \omega, R)$ for $q = 15$ with argon in both gas targets, corresponding to a 2D interferogram in the (z_1, z_2) domain. The structure of this interferogram can be understood by considering a simple model of the fringe spacing in this domain. Using equation 1 the on-axis phase difference near the beam waist in the case of both targets containing the same gas species can be approximated as

$$\Delta\phi_q(z_1, z_2) \approx q\frac{(z_2 - z_1)}{z_R} + \alpha_q^s \frac{I_0}{z_r^2}\left(z_2^2 - z_1^2\right), \tag{2}$$

where I_0 is the on-axis peak intensity at the focal plane and α_q^s reflects the dominance of the short-trajectory component of the harmonic emission to the on-axis harmonic spectrum [35]. Close to the focal region, the laser intensity varies slowly with longitudinal position such that the phase difference between harmonics generated in both targets is dominated by the first term in equation (2), which varies approximately linearly across this region as a result of the use of an appropriately sized aperture before the focusing lens. In this simple model, the fringe period scales as $\sim z_R/q$. As a result, clear diagonal fringes are observed in the (z_1, z_2) domain over the full range of measured longitudinal positions, with the spacing between fringes decreasing for increasing harmonic order.

The simple model described by equation (2) is useful for understanding the scaling and general structure of the interferograms. However, in order to develop a more complete model of the interferometer, simulations were performed that incorporated numerical propagation of the laser beam, as well as a semi-classical model of harmonic emission from both sources based on the strong-field approximation (SFA) [36]. The simulations were performed for a pulse duration of 40 fs, peak laser intensity at the focus after clipping of 1.6×10^{14} Wcm^{-2} with an effective Rayleigh range of 8.6 mm and a hydrogen-like dipole with ionization potential 15.76 eV. The longitudinal and transverse structure of the laser beam within the focal region was calculated using the angular spectrum method, assuming an azimuthally symmetric beam, and taking into account the effect of clipping by the mechanical iris. The harmonic emission from each gas cell, taken as the single-atom response over a plane and incorporating the transverse extent of the driving field, was then calculated using the SFA model. The harmonic fields from both targets were propagated to the detector plane using the Fresnel diffraction integral, where they were summed to yield the spatio-spectrally resolved harmonic profile. The full $\mathcal{I}(z_1, z_2, \omega, R)$ interferogram was then simulated by repeating the calculation for each target position. Interferograms were simulated over $z_1, z_2 = \pm 12$ mm for the case of argon in both gas targets and the results for the on-axis component for harmonics orders $q = 17 - 25$ are shown in figure 2(bottom row). The yellow-shaded area corresponds to the (z_1, z_2) region that could be

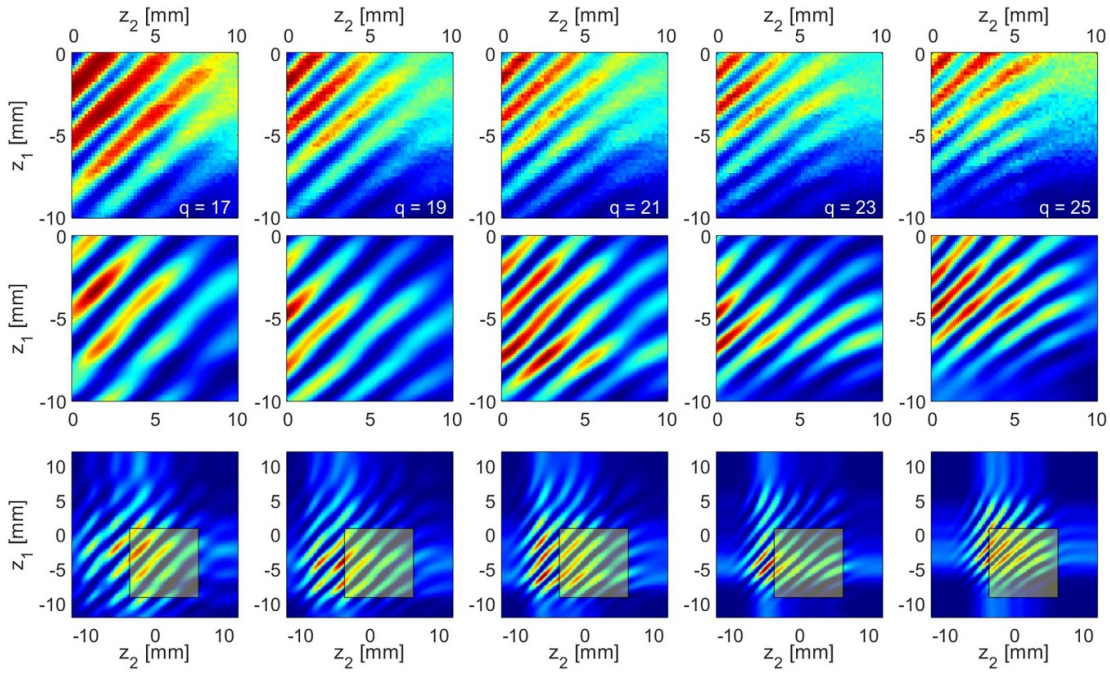

Figure 2. Measured (top row) and simulated (middle row) on-axis interferograms for $q = 17 - 25$ with argon in both targets. Simulated (bottom row) interferograms over $z_{1,2} = \pm 12$ mm with the yellow-shaded region corresponding to the data shown in the middle row and highlighting the experimentally accessible region in this experiment. Note, the $z_{1,2}$ offset between the simulated and measured interferograms has been removed for the interferograms shown in the middle row.

measured in this experiment and is shown separately in figure 2(middle row) for clarity. The measured on-axis interferograms for harmonic orders $q = 17 - 25$ are shown in figure 2(top row). Excellent agreement between the measured and simulated interferograms is observed over all harmonic orders. Both measured and simulated interferograms exhibit clear diagonal fringes across all harmonic orders with decreasing fringe spacing for increasing values of q. For harmonics in the cutoff region ($q > 21$) the measured fringes are observed to bend slightly at large values of z_1 and z_2. This behaviour, which is also observed in the simulated interferograms, is due to the increasing value of α_q^s towards the harmonic cutoff [37], which increases the contribution of the quadratic phase term in equation 2 and leads to curvature of the fringes in the (z_1, z_2) domain at large target separations. The use of thin-walled tubes as gas targets currently limits the experimentally accessible region of the (z_1, z_2) domain to that highlighted by the yellow boxes in figure 2(bottom row). However, alternative gas delivery systems, such as gas jets, could be employed to access a larger region of the (z_1, z_2) domain.

The behaviour in the radial dimension can be observed by considering consecutive (z_1, z_2) interferograms along the R domain, a selection of which are shown in figure 1(e) (additional data in supplementary material). It is seen that in off-axis regions the structure of the interferogram becomes significantly more complex, departing from the simple diagonal fringe patterns observed on-axis. This is the result of an increasing contribution from the long-trajectory components of the harmonic emission, which exhibit a larger divergence due to the longer transit times of electrons in the continuum and consequently larger transverse phase variation at the generation plane [35]. In transverse regions where the short and long trajectory components have approximately equal contributions to the measured spectrum, such as at $R \approx 1$ mm in figure 1(e), the interferogram becomes highly structured due to interference between the overlapping contributions of the different trajectory components from both gas targets [38]. Qualitative agreement of this complex structure between measured and simulated interferograms is observed across all harmonics (see supplementary data) providing strong evidence that the distortions in the fringe patterns are due to the relative contributions of the different trajectory components of the harmonic emission. A detailed discussion of the structure of the interferograms in the radial co-ordinate and its dependence on quantum trajectories will be provided in a separate publication. In the rest of this paper analysis is restricted to the on-axis ($R = 0$) component of the harmonic emission which is dominated by the short-trajectory component, simplifying analysis and interpretation of the observed interferograms.

The inherent stability of this setup allows the Ar−Ar interferograms to be used as a highly stable reference to perform differential phase measurements. Previously, differential phase measurements using HHG-based interferometry have been employed to resolve the photorecombination dipole phase difference

between neon and helium, as well as the photorecombination dipole phase around the Cooper minimum of argon [24]. This scheme makes use of the factorization of the HHG process in which the harmonic yield can be expressed as the product of recolliding electron wavepackets, governed by the driving laser field, and the photorecombination cross-section of the generating species [39, 40], allowing the harmonic phase to be expressed as the sum of the phases acquired during the strong-field driven processes of ionization and propagation and the phase at photorecombination. Comparing HHG interferograms obtained under identical driving laser conditions and removing the strong-field contribution to the harmonic phase then allows the dipole phase difference between a target and reference atom to be measured.

In the current setup, for the case of argon in both targets, the on-axis phase difference according to equation (1) is given by

$$\Delta\phi_q^{\text{Ar-Ar}}(z_1,z_2) = q\left(\phi_{\text{G}}(z_1) - \phi_{\text{G}}(z_2)\right) + \alpha_q^{\text{s,Ar}}\left(I(z_1) - I(z_2)\right). \tag{3}$$

Replacing the gas in the second target and repeating the scan under identical driving laser conditions yields a separate interferogram the on-axis phase difference of which is given by

$$\Delta\phi_q^{\text{Ar-X}}(z_1,z_2) = q\left(\phi_{\text{G}}(z_1) - \phi_{\text{G}}(z_2)\right) + \left(\alpha_q^{\text{s,Ar}} I(z_1) - \alpha_q^{\text{s,X}} I(z_2)\right) + \left(\psi_q^{\text{Ar}} - \psi_q^{X}\right) \tag{4}$$

where X is the gas species in the second target. Taking the difference between $\Delta\phi_q^{\text{Ar-Ar}}(z_1,z_2)$ and $\Delta\phi_q^{\text{Ar-X}}(z_1,z_2)$ yields the absolute phase difference between harmonics generated in the target and the argon reference gas

$$\Phi_q^{X}(z_1,z_2) = I(z_2)\left(\alpha_q^{\text{s,X}} - \alpha_q^{\text{s,Ar}}\right) + \left(\psi_q^{\text{Ar}} - \psi_q^{X}\right). \tag{5}$$

Taking the difference therefore removes the common contributions due to the Gouy phase and the longitudinal intensity variation in the first target. The first term in equation 5 is the phase difference due to the different transit times experienced by the electron wavepackets from the target and reference gases during the propagation phase of HHG. It is noted that although α_q^s is simply due to classical acceleration from the laser field it is not the same for both targets owing to the change in ionization time (due to tunnelling through a different barrier). The second term in equation (5) accounts for the phase difference between the target and reference gases due to both ionization and photorecombination. Consequently, the differential phase that is extracted, $\Phi_q(z_1,z_2)$, is related to all stages of the HHG process: ionization, propagation and recombination.

To perform differential measurements, a series of scans were performed under identical driving laser conditions for a range of atomic and molecular gases in the second target while leaving the argon in the first target unchanged. We note that the reference gas does not need to be argon. For example, differential measurements have previously been demonstrated using neon as a reference gas in order to exploit its relatively flat dipole phase in the region of the Cooper minimum of argon [24]. For each scan, the amplitude and phase of the on-axis component of the reference and target interferograms was extracted for each harmonic order using bandpass filtering [41] to yield the complex quantities $Z_q^X(z_1,z_2)$ and $Z_q^{\text{Ar}}(z_1,z_2)$ for the target and reference gases. The resulting 2D complex interference amplitude

$$\tilde{Z}_q^X(z_1,z_2) = Z_q^X(z_1,z_2)\left[Z_q^{\text{Ar}}(z_1,z_2)\right]^* \tag{6}$$

was then calculated (see supplementary material). The results of these measurements are summarized in figure 3, which show $[\rho_q^X(z_1,z_2), \Phi_q^X(z_1,z_2)] = [|\tilde{Z}_q^X(z_1,z_2)|, \arg(\tilde{Z}_q^X(z_1,z_2)]$ for each harmonic order and gas species combination. Each data point in figure 3 corresponds to the value of the complex interference amplitude for a particular harmonic order and gas combination at a single (z_1,z_2) position; points of the same colour are from the same gas-species combination. It is seen that the data for each harmonic order is distributed into well-defined bands, demonstrating a clear phase relationship across all (z_1,z_2) positions. The angle of each band yields the absolute phase difference between the harmonic emission from the target and reference gases, according to equation 5. For each harmonic order in figure 3, the amplitude corresponds to the strength of the signal and has been normalized to the maximum amplitude of $\tilde{Z}_q^X(z_1,z_2)$ for that harmonic order across all gas combinations. A clear signal was observed in all cases with the exception of the xenon-argon combination, which only exhibited clearly resolvable fringes up to $q = 19$ (see supplementary material) due to the lower ionization potential, and consequently lower harmonic cut-off, of xenon. A clear rotation of the phase angle is observed for increasing harmonic order for all gas combinations with the rotation direction being different for atoms (anti-clockwise) and molecules (clockwise). This rotation is due to the well-known chirp of harmonic emission and the opposite rotation direction indicating that, relative to emission from argon under the same laser conditions, harmonic emission occurs earlier in the atomic systems investigated and later in the molecular systems. As discussed below, it has been demonstrated that harmonic emission from molecules is sensitive to structural and dynamical effects [12], that may result in

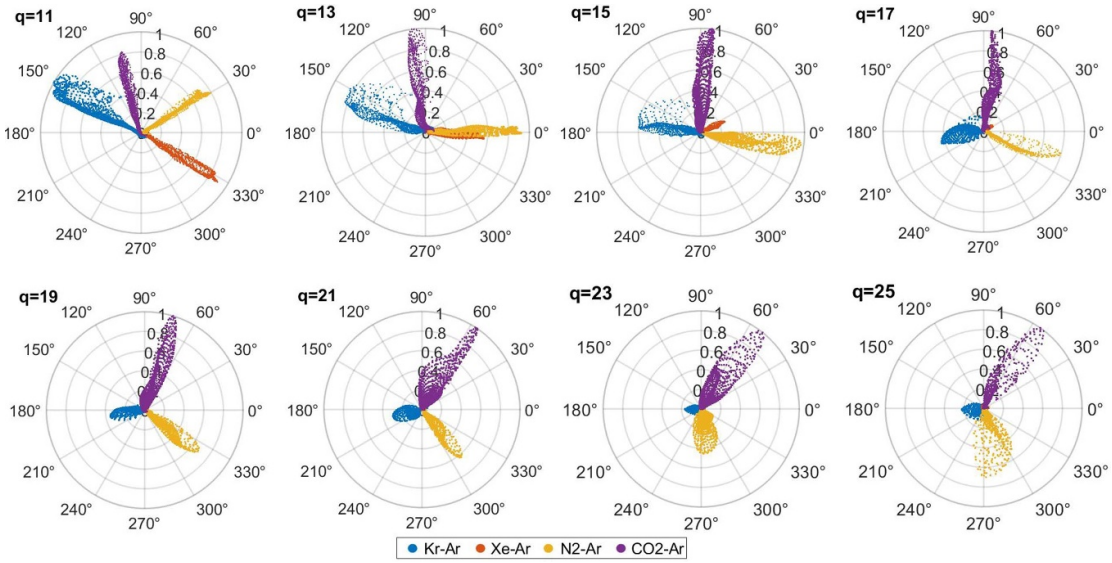

Figure 3. Polar plots showing the differential interferometric complex amplitude $\tilde{Z}_q^X(z_1, z_2)$ for all harmonic orders and gas combinations used in the experiment. The radial co-ordinate indicates the strength of the interferometric term and the angle the differential phase. The angular spread can be used to determine the precision of the measurement. Each data point corresponds to the amplitude and phase of the interferometric contribution at a given pair of target positions, all points of a given colour correspond to all target position pairs for a given gas combination.

earlier harmonic emission. Extending these measurements to a wider range of molecular gases will be the subject of future experiments.

For each target gas, the differential phase, $\Phi_q^X(z_1, z_2)$, was extracted by calculating the weighted mean of the corresponding band of data points shown in figure 3. The resulting differential phase extracted for each harmonic order and target gas species is shown in figure 4. The associated error, illustrated by the shaded region in figure 4, was taken as the standard deviation of the data points from the weighted mean. The average error across all harmonics measured was 65 mrad (corresponding to a temporal resolution of approximately 1 as at the centre energy of the measured harmonics), demonstrating that extremely precise phase measurements can be performed with this approach. This precision was afforded by the 4D data set: spatially-spectrally resolving the harmonics allows for a single trajectory to be isolated, and the 2D longitudinal scan allows for more refined bandpass filtering and higher redundancy (i.e. more independent data points) compared to a 1D longitudinal scan. The phase difference was observed to vary approximately linearly across all harmonics measured. The gradient of the linear fits (dashed lines) shown in figure 4 therefore corresponds to the average delay, $\Delta\tau$, in the emission of the attosecond pulse train from the corresponding gas relative to argon and is summarized in table 1. It is seen that emission from the atomic systems Xe and Kr occurs earlier ($\Delta\tau < 0$) relative to emission from Ar while relative emission occurs later ($\Delta\tau > 0$) for CO_2 and N_2. The inline nature of the interferometer allows precise measurement of the emission delays with a standard deviation of approximately 5 as across the gas combinations investigated. We note that this precision is significantly better than the sampling limit from the bandwidth of the measurements ($\delta t = \frac{2\pi}{\Delta\omega} = \frac{2\pi}{\Delta q\omega_0} = 188$ as) and that such few attosecond accuracy compares very well with recent experiments to probe the dipole response of HHG using XUV ellipsometry [42] as well as previous Gouy-based interferometry measurements of the harmonic phase difference between isotopes of molecular hydrogen [30].

Varying the gas species in the second target changes I_p which leads to variation in all three stages of the HHG process: ionization, continuum dynamics and photorecombination. After tunnel ionization the electron emerges into the continuum at time t_i with approximately zero momentum ($p_e \approx 0$) at a position $r_e(t_i) \approx I_p/|E_L(t_i)|$, where $E_L(t)$ is the laser field strength, such that the initial conditions of the electron are approximately independent of the core potential. Since the electric field of the laser is significantly stronger than that of the parent ion, the contribution of the core's potential to the ionized electron can be neglected and subsequent dynamics of the electron are predominantly determined by the laser field with the electron returning to the vicinity of the core at a later time t_r with non-zero momentum ($p_e = \omega_q - I_p$). The delay times extracted from the differential phase are therefore dominated by the contributions due to the laser-driven propagation in the continuum and photorecombination.

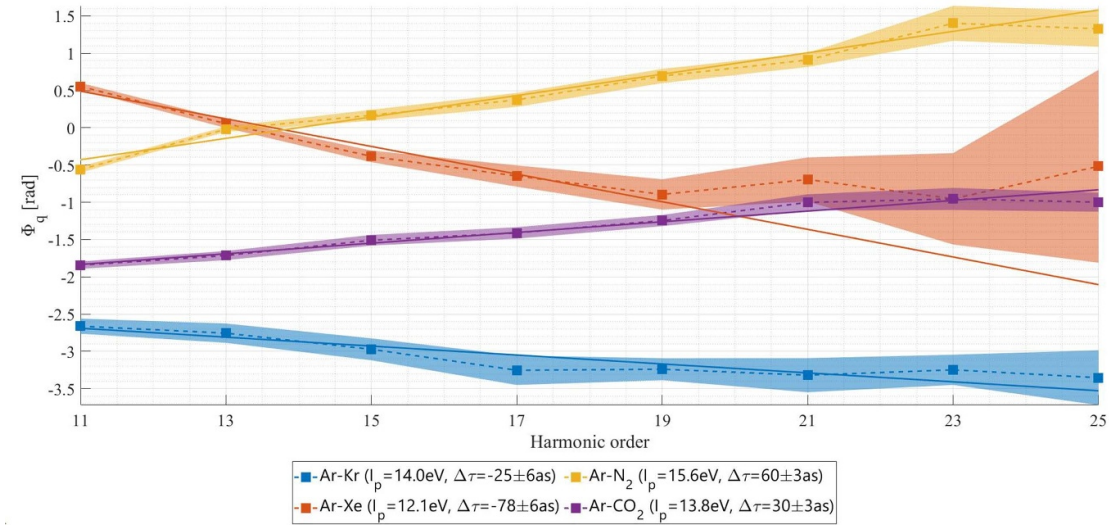

Figure 4. Measured phase difference (squares and dashed line) between target gas and argon reference and linear fit to data (solid line). The shaded regions correspond to the error calculated from the spread of the corresponding data shown in figure 3.

Table 1. Measured delay in harmonic emission relative to emission from argon reference.

Gas in target 2	I_P (eV)	$\Delta\tau$ (as)
Xe	12.1	-78 ± 6
Kr	14.0	-25 ± 6
CO_2	13.8	30 ± 3
N_2	15.6	60 ± 3

Over the range of harmonic orders observed in this experiment, delays in harmonic emission relative to argon of $\Delta\tau = -25 \pm 6$ as and $\Delta\tau = -78 \pm 6$ as were measured for Kr and Xe, respectively. To estimate the propagation delay due to the difference in ionization potential relative to argon (ΔI_p) the classical trajectories of the electron after ionization were calculated for different ionization potentials. Return times after argon of 35 as and 72 as were calculated for Kr ($\Delta I_p = 1.76$ eV) and Xe ($\Delta I_p = 3.63$ eV), respectively. These values are similar to the absolute values of the measured delays, indicating that the continuum dynamics can contribute significantly to the measured delays.

To estimate the delay due to ionization and photorecombination the relative delay was simulated using the SFA for a range of different ground-state hygrogen-like orbitals with fixed ionization potential $I_p = 15.759$ eV (i.e. that of Argon). The on-axis phase of harmonics in the far-field for 1*s*, 2*s*, 2*p*, 3*s* and 3*p* orbitals was calculated with resulting delays ranging from $\Delta\tau = -13$ as for the 1*s*–2*s* orbitals to $\Delta\tau = -117$ as for the 1*s*–3*s* orbitals (see supplementary material). These simulations indicate that the delays extracted in our interferometric measurements are comparable to the delays caused by the change in orbital structure. This, combined with the fact that we measured positive delays for molecules and negative delays for larger atoms, is strong evidence for the sensitivity of this technique to the orbital structure of the parent species.

The differential phase was also extracted for unaligned CO_2 and N_2. The resulting delays in emission relative to the Ar reference were $\Delta\tau = 30 \pm 3$ as for CO_2 and $\Delta\tau = 60 \pm 3$ as for N_2, indicating the harmonics are emitted later from the molecular gases tested relative to emission from Ar. Harmonic emission from molecules is expected to be more complex than the case of atoms. Both electronic and nuclear dynamics are present between ionization and recombination, as well as the contribution from several electronic states of the molecular ion. For example, using two-slit interferometry to measure the relative phase between harmonic emission from aligned and unaligned CO_2 it has been shown that the highest occupied molecular orbital (HOMO), HOMO-1 and HOMO-2 all contribute to high harmonic emission resulting in strong phase variation between harmonics depending on the relative contributions of the various channels [12]. In figure 4, the measured phase difference between CO_2 and Ar is seen to vary smoothly across the full range of harmonics observed. However, in contrast with Smirnova *et al* [12], the target gas in this experiment is a randomly aligned molecular ensemble and the angle-dependent contributions from the different channels are smeared out. Thus, we do not expect to be sensitive to phase variations originating

from the different contributing orbitals. However, the setup used in this experiment is naturally compatible with alignment experiments and will be the subject of a future experiment. Indeed, since the target and reference gases are longitudinally separated, arbitrary reference gases can be used, in contrast with conventional two-slit interferometry where both sources are transversely separated in a single gas jet, allowing independent control of the reference species and signal (via pressure tuning). Such control may prove useful in performing interferometry on complex systems where use of a reference atom with well-known dipole phase may be beneficial.

For N_2, both the target and reference gas have similar ionization potentials ($\Delta I_p = 0.18$ eV) resulting in near identical intensity-dependent ionization probabilities [43–45]. As a result, the ionization and propagation steps of the HHG process are the same in both gases. In this case, the extracted phase difference is given by

$$\Phi_q(z_1, z_2) \approx \left(\psi^{\mathrm{Ar}}_{\mathrm{rec},q} - \psi^{\mathrm{N_2}}_{\mathrm{rec},q}\right) \tag{7}$$

and is the absolute photorecombination phase difference between argon and N_2. The photorecombination phase is an important parameter for tomographic imaging. In previous experiments imaging the HOMO of N_2 [7], the phase values needed for reconstruction were assumed based on calculations [46]. In our experiment, the phase difference is accessed directly. Combined with molecular alignment, this opens the possibility of time-resolved tomographic imaging of molecules in a simple experimental arrangement.

4. Conclusion

Multi-dimensional HHG-based Gouy interferometry has been demonstrated as a method for accessing the absolute phase difference of harmonic emission from atomic and molecular gases, allowing relative emission times to be measured with single-digit attosecond precison. This scheme is straightforward to implement in existing HHG setups that use free-focus geometries and opens new opportunities for probing electronic wavefunctions. Future experiments will focus on using this technique to probe phase variations around Cooper minima and atomic resonances, as well as to resolve the phase of harmonics generated in aligned molecular gases. More generally, the multi-dimensional nature of this measurement provides data sets that are significantly richer than those retrieved in other HHG interferometry techniques. Modelling based on the SFA yields excellent agreement between the simulated and measured interferograms for the case of argon in both targets. However, extending modelling to molecular systems, particularly in the case of alignment systems where a host of structural and dynamical effects can be observed, has the potential to provide new insight into molecular dynamics, as well as to act as a robust test of underpinning theoretical models.

Data availability statement

Data stored on CLF repository. The data that support the findings of this study are available upon reasonable request from the authors.

Acknowledgments

This work was supported by EPSRC (EP/N029313/1).

Conflicts of interest

The authors declare no conflicts of interest.

ORCID iDs

Adam S Wyatt https://orcid.org/0000-0001-8625-6709
Richard T Chapman https://orcid.org/0000-0002-4622-8305
Christopher Thornton https://orcid.org/0000-0003-1267-5788
Paulina Majchrzak https://orcid.org/0000-0002-5200-3866
Alfred J H Jones https://orcid.org/0000-0002-7930-0967
Emma Springate https://orcid.org/0000-0002-9121-3698
Kevin O'Keeffe https://orcid.org/0000-0003-2085-0806

References

[1] Krausz F and Ivanov M 2009 Attosecond physics *Rev. Mod. Phys.* **81** 163–234
[2] Marangos J P 2016 Development of high harmonic generation spectroscopy of organic molecules and biomolecules *J. Phys. B: At. Mol. Opt. Phys.* **49** 132001
[3] Li J, Lu J, Chew A, Han S, Jialin Li, Wu Y, Wang H, Ghimire S and Chang Z 2020 Attosecond science based on high harmonic generation from gases and solids *Nat. Commun.* **11** 2748
[4] Corkum P B 1993 Plasma perspective on strong field multiphoton ionization *Phys. Rev. Lett.* **71** 1994–7
[5] Baker S, Robinson J S, Haworth C A, Teng H, Smith R A, Chirila C C, Lein M, Tisch J W G and Marangos J P 2006 Probing proton dynamics in molecules on an attosecond time scale *Science* **312** 424–7
[6] Lein M 2005 Attosecond probing of vibrational dynamics with high-harmonic generation *Phys. Rev. Lett.* **94** 053004
[7] Itatani J, Levesque J, Zeidler D, Niikura H, Pépin H, Kieffer J C, Corkum P B and Villeneuve D M 2004 Tomographic imaging of molecular orbitals *Nature* **432** 867
[8] Haessler S *et al* 2010 Attosecond imaging of molecular electronic wavepackets *Nat. Phys.* **6** 200–6
[9] Jakob Wörner H *et al* 2017 Charge migration and charge transfer in molecular systems *Struct. Dyn.* **4** 061508
[10] Kraus P M *et al* 2015 Measurement and laser control of attosecond charge migration in ionized iodoacetylene *Science* **350** 790–5
[11] Saito N, Sannohe H, Ishii N, Kanai T, Kosugi N, Wu Y, Chew A, Han S, Chang Z and Itatani J 2019 Real-time observation of electronic, vibrational and rotational dynamics in nitric oxide with attosecond soft x-ray pulses at 400 ev *Optica* **6** 1542–6
[12] Smirnova O, Mairesse Y, Patchkovskii S, Dudovich N, Villeneuve D, Corkum P, Misha Y I 2009 High harmonic interferometry of multi-electron dynamics in molecules *Nature* **460** 972–7
[13] Lloyd D T, O'Keeffe K and Hooker S M 2013 Complete spatial characterization of an optical wavefront using a variable-separation pinhole pair *Opt. Lett.* **38** 1173
[14] Lloyd D T, O'Keeffe K, Anderson P N and Hooker S M 2016 Gaussian-schell analysis of the transverse spatial properties of high-harmonic beams *Sci. Rep.* **6** 30504
[15] Austin D R, Witting T, Arrell C A, Frank F, Wyatt A S, Marangos J P, Tisch J W G and Walmsley I A 2011 Lateral shearing interferometry of high-harmonic wavefronts *Opt. Lett.* **36** 1746–8
[16] Cormier E, Walmsley I A, Kosik E M, Wyatt A S, Corner L and DiMauro L F 2005 Self-referencing, spectrally, or spatially encoded spectral interferometry for the complete characterization of attosecond electromagnetic pulses *Phys. Rev. Lett.* **94** 033905
[17] Mang M M, Bourassin-Bouchet C and Walmsley I A 2014 Simultaneous spatial characterization of two independent sources of high harmonic radiation *Opt. Lett.* **39** 6142–5
[18] Corsi C, Pirri A, Sali E, Tortora A and Bellini M 2006 Direct interferometric measurement of the atomic dipole phase in high-order harmonic generation *Phys. Rev. Lett.* **97** 023901
[19] Bellini M, Lyngå C, Tozzi A, Gaarde M B, Hänsch T W, L'Huillier A and Wahlström C-G 1998 Temporal coherence of ultrashort high-order harmonic pulses *Phys. Rev. Lett.* **81** 297–300
[20] Kanai T, Takahashi E J, Nabekawa Y and Midorikawa K 2007 Destructive interference during high harmonic generation in mixed gases *Phys. Rev. Lett.* **98** 153904
[21] Dudovich N, Smirnova O, Levesque J, Mairesse Y, Yu Ivanov M, Villeneuve D M and Corkum P B 2006 Measuring and controlling the birth of attosecond XUV pulses *Nat. Phys.* **2** 781–6
[22] Isinger M, Busto D, Mikaelsson S, Zhong S, Guo C, Saliéres P, Arnold C L, L'Huillier A and Gisselbrecht M 2019 Accuracy and precision of the rabbit technique *Phil. Trans. R. Soc.* A **377** 20170475
[23] Bertrand J B, Wörner H J, Salières P, Villeneuve D M and Corkum P B 2013 Linked attosecond phase interferometry for molecular frame measurements *Nat. Phys.* **9** 174–8
[24] Azoury D, Kneller O, Rozen S, Bruner B D, Clergerie A, Mairesse Y, Fabre B, Pons B, Dudovich N and Krüger M 2019 Electronic wavefunctions probed by all-optical attosecond interferometry *Nat. Photon.* **13** 54–59
[25] Shafir D, Soifer H, Bruner B D, Dagan M, Mairesse Y, Patchkovskii S, Yu Ivanov M, Smirnova O and Dudovich N 2012 Resolving the time when an electron exits a tunnelling barrier *Nature* **485** 343
[26] Kneller O *et al* 2022 A look under the tunnelling barrier via attosecond-gated interferometry *Nat. Photon.* **16** 304–10
[27] Azoury D, Krüger M, Bruner B D, Smirnova O and Dudovich N 2021 Direct measurement of coulomb-laser coupling *Sci. Rep.* **11** 495
[28] Azoury D, Kneller O, Krüger M, Bruner B D, Cohen O, Mairesse Y and Dudovich N 2019 Interferometric attosecond lock-in measurement of extreme-ultraviolet circular dichroism *Nat. Photon.* **13** 03
[29] Laban D E *et al* 2012 Extreme ultraviolet interferometer using high-order harmonic generation from successive sources *Phys. Rev. Lett.* **109** 263902
[30] Hena Mustary M, Liang X, Wanyang W, Haram N, Laban D E, Han X, Feng He, Sang R T and Litvinyuk I V 2022, Attosecond delays of high-harmonic emissions from hydrogen isotopes measured by XUV interferometer *Ultrafast Sci.* **2022** 9834102
[31] Mang M M, Lloyd D T, Anderson P N, Treacher D, Wyatt A S, Hooker S M, Walmsley I A and O'Keeffe K 2018 Spatially resolved common-path high-order harmonic interferometry *Opt. Lett.* **43** 5275–8
[32] Lewenstein M, Salières P and L'Huillier A 1995 Phase of the atomic polarization in high-order harmonic generation *Phys. Rev.* A **52** 4747–54
[33] Balcou P, Salières P, L'Huillier A and Lewenstein M 1997 Generalized phase-matching conditions for high harmonics: the role of field-gradient forces *Phys. Rev.* A **55** 3204–10
[34] Heyl C M, Güdde J, Höfer U and L'Huillier A 2011 Spectrally resolved maker fringes in high-order harmonic generation *Phys. Rev. Lett.* **107** 033903
[35] Catoire F, Ferré A, Hort O, Dubrouil A, Quintard L, Descamps D, Petit S, Burgy F, Mével E, Mairesse Y and Constant E 2016 Complex structure of spatially resolved high-order-harmonic spectra *Phys. Rev.* A **94** 063401
[36] Lewenstein M, Balcou Ph, Ivanov Yu M, Huillier Anne L and Corkum P B 1994 Theory of high-harmonic generation by low-frequency laser fields *Phys. Rev.* A **49** 2117–32
[37] Varjú K *et al* 2005 Frequency chirp of harmonic and attosecond pulses *J. Mod. Opt.* **52** 379–94
[38] Zaïr A *et al* 2008 Quantum path interferences in high-order harmonic generation *Phys. Rev. Lett.* **100** 143902
[39] Frolov M V, Manakov N L, Sarantseva T S and Anthony F S 2011 Analytic confirmation that the factorized formula for harmonic generation involves the exact photorecombination cross section *Phys. Rev.* A **83** 043416
[40] Anh-Thu L, Morishita T and Lin C D 2008 Extraction of the species-dependent dipole amplitude and phase from high-order harmonic spectra in rare-gas atoms *Phys. Rev.* A **78** 063824

[41] Takeda M, Ina H and Kobayashi S 1982 Fourier-transform method of fringe-pattern analysis for computer-based topography and interferometry *J. Opt. Soc. Am.* **72** 156–60
[42] Chang K-Y, Huang L-C, Asaga K, Tsai M-S, Rego L, Huang P-C, Mashiko H, Oguri K, Hernández-García C and Chen M-C 2021 High-order nonlinear dipole response characterized by extreme ultraviolet ellipsometry *Optica* **8** 484–92
[43] Liang Y, Augst S, Chin S L, Beaudoin Y and Chaker M 1994 High harmonic generation in atomic and diatomic molecular gases using intense picosecond laser pulses-a comparison *J. Phys. B: At. Mol. Opt. Phys.* **27** 5119
[44] Otobe T, Yabana K and Iwata J-I 2004 First-principles calculations for the tunnel ionization rate of atoms and molecules *Phys. Rev.* A **69** 053404
[45] Wabnitz H *et al* 2006 Generation of attosecond pulses in molecular nitrogen *Eur. Phys. J.* D **40** 305–11
[46] Hay N, Lein M, Velotta R, De Nalda R, Heesel E, Castillejo M, Knight P L and Marangos J P 2003 Investigations of electron wave-packet dynamics and high-order harmonic generation in laser-aligned molecules *J. Mod. Opt.* **50** 561–77